Astron. Astrophys. 333, 702–708 (1998)

ASTRONOMY AND ASTROPHYSICS

Far-infrared ISOPHOT observations and the energy balance of a quiescent globule⋆

K. Lehtinen[1], **D. Lemke**[2], **K. Mattila**[1], **and L.K. Haikala**[1]

[1] Observatory, P.O. Box 14, FIN-00014 University of Helsinki, Finland
[2] Max-Planck-Institut für Astronomie, Königstuhl 17, D-69117 Heidelberg, Germany

Received 6 October 1997 / Accepted 20 January 1998

Abstract. We have observed a quiescent small globule, the Thumbprint Nebula, with the ISOPHOT far-infrared camera at 100 and 200μm. The observed emission is optically thin thermal emission from dust at a temperature of ∼14–16 K. The energy budget of the cloud is studied by considering the energy input (interstellar radiation field, ISRF), and outputs (scattered and emitted radiation). It is found that the ISRF is sufficient to be the only heating source of dust in the cloud. We have derived values of absorption cross sections of dust at 100 and 200μm, and found them to be in good agreement with current dust models.

Key words: ISM: clouds – dust, extinction – ISM: individual objects: Thumbprint Nebula – infrared: ISM: continuum

1. Introduction

Globules provide examples of dense and cold interstellar dust clouds which often have a simple and regular structure and are, therefore, ideal objects for studies of the heat balance and the dust grain properties. Far-infrared observations are especially suited to study the emission by large grains which are thought to cause most of the optical extinction. Previous far-IR observations of globules (Keene et al. 1980, 1983; Keene 1981; Clemens et al. 1991; Yun & Clemens 1991) have suffered either from atmospheric limitations, insufficient spatial resolution or limited wavelength coverage.

The Thumbprint Nebula (hereafter TPN) is a small, highly symmetric Bok globule located in the Chamaeleon III region. The TPN has been previously studied at millimeter, optical and near-infrared wavelengths. The millimeter CO isotopic observations of Lehtinen et al. (1995) show that the mass of the TPN is $\sim 6\,M_\odot$, and the temperature of the molecular gas is ~ 7 K. At optical and near-IR wavelengths the TPN shows a surface brightness higher than the adjacent background sky. This surface brightness is due to the diffuse interstellar radiation scattered by dust grains in the TPN. The photometry of the surface brightness of the TPN and of background stars have enabled the determination of dust scattering properties and the optical depth at optical (FitzGerald et al. 1976) and near-IR wavelengths (Lehtinen & Mattila 1996).

The TPN shows no signs of star formation; thus it is heated mainly by the interstellar radiation field (ISRF). The TPN is just detectable at 60 and 100 μm in IRAS images (Lehtinen et al. 1995), but the angular resolution is not sufficient to reveal the structure of the TPN.

The ISOPHOT cameras onboard ISO (Infrared Space Observatory) offer a better angular resolution and an extended long-wavelength capacity. In order to study the temperature and distribution of cold dust in the TPN, we have made observations at far-IR wavelengths where the surface brightness of the cloud is caused by equilibrium emission of dust grains.

As shown by Keene (1981) the integrated mean radiation density of the ISRF can be checked observationally. A quiescent globule with no internal energy sources and of sufficiently large optical depth at optical/near-IR wavelengths will remove almost all the intercepted radiation from the ISRF and return it as either thermal far-IR emission or optical/near-IR scattered light. The situation has been puzzling since the emitted radiation alone (without accounting for the scattered part) from a sample of globules (Keene 1981) has exceeded the estimated ISRF density (for a review see Mezger 1991). With the ISOPHOT mapping data we are now in the position to cover essentially the whole FIR emission from the TPN, both spatially, and in wavelength. Complemented with data on the scattered light component we are able for the first time to present an accurate assessment of the total energy budget of a quiescent globule.

Table 1. Observational parameters. The d_{Airy} is the diameter of the Airy disk at λ_c

Filter	λ_c [μm]	$\Delta\lambda$ [μm]	d_{Airy} [″]	Pixel size [″]	Map size [′]
C_100	103.5	43.6	83.9	43.5×43.5	16×16
C_200	204.6	67.3	168	89.4×89.4	15×15

Send offprint requests to: K. Lehtinen

⋆ Based on observations with ISO, an ESA project with instruments funded by ESA Member States (especially the PI countries: France, Germany, the Netherlands and the United Kingdom) and with the participation of ISAS and NASA

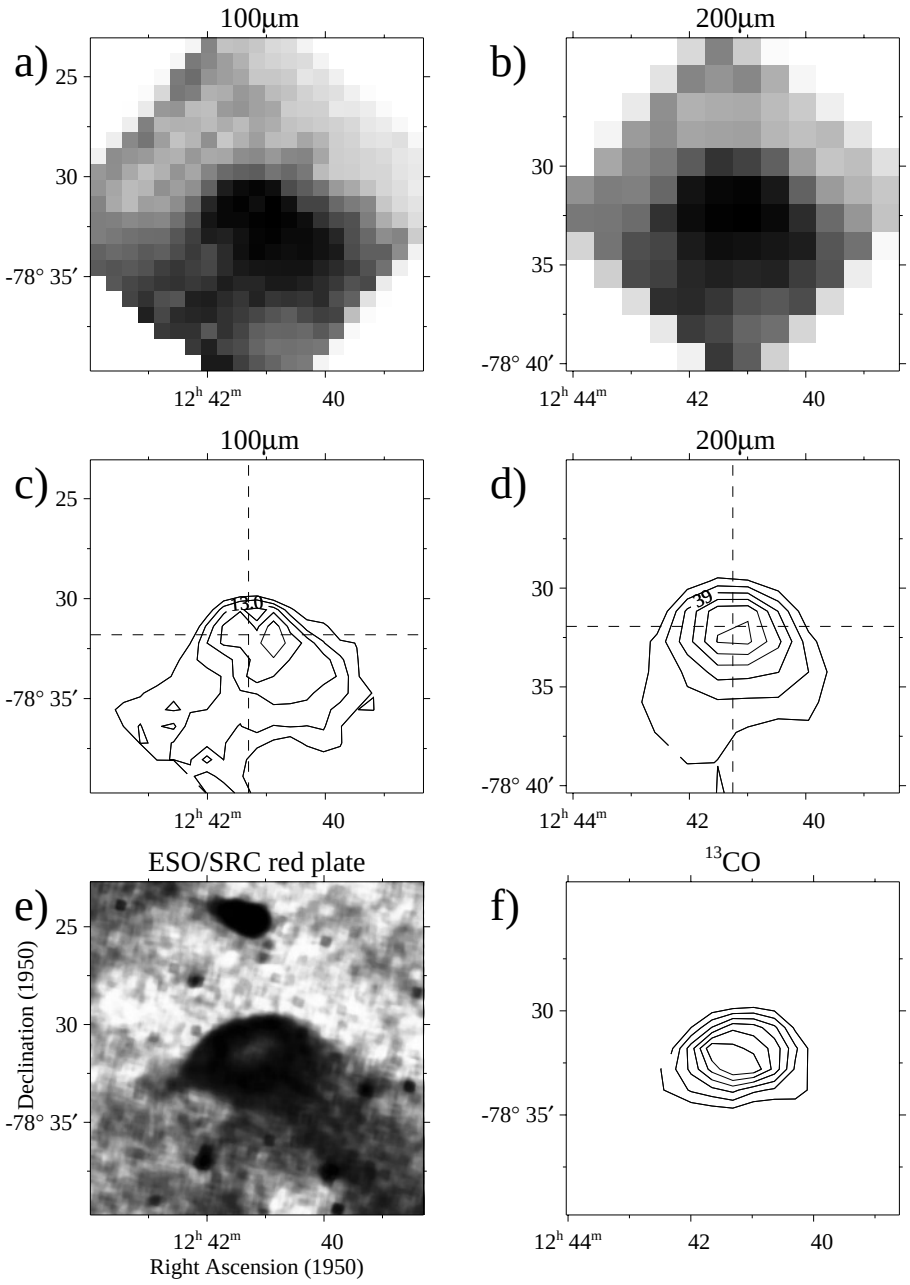

Fig. 1a–f. Greyscale and contour plots of the surface brightness at 100 μm (**a,c**) and 200 μm (**b,d**). The contour levels are from 12 to 14 by 0.5 MJy sr^{-1} at 100 μm, and from 33 to 48 by 3 MJy sr^{-1} at 200 μm. The dashed lines mark the positions of the profiles shown in the Fig. 2. In panel **e** is shown the grayscale image of the surface brightness at R-band (ESO/SRC red Sky Survey Plate), and in the panel **f** is shown the ^{13}CO(J=1–0) column density contour map

2. Observations

The observations have been made with the ISOPHOT C100 and C200 cameras (Lemke et al. 1996) at nominal wavelengths of 100 μm and 200 μm, respectively. The observing mode used was observation template PHT 22, i.e. a raster map on a two-dimensional regular grid. At 100 μm the grid spacings in in-scan and cross-scan directions were 135″ and 90″, respectively. At 200 μm the grid spacing was 180″ in both directions. The observational specifications are given in Table 1.

3. Data processing

The data reduction was done in a standard way, using the ISOPHOT Interactive Analysis (PIA) tool (Gabriel et al. 1996) version 6.1. The integration ramps were first corrected for detector nonlinearities and glitches caused by cosmic ray particle hits. Then the ramps were fitted with a polynomial of degree one, and the dark current was subtracted.

In order to make a flatfield correction for the C_100 map we have plotted for each pixel its values against the values of a reference pixel, using all the raster positions in the map, and used these relations to derive the correction. The C_200 map does not have enough pixels to use this method, thus we have used a smooth background region to derive the flatfield correction.

The calibration of the data is based on the fine calibration sources aboard the ISOPHOT. Since this internal calibration is

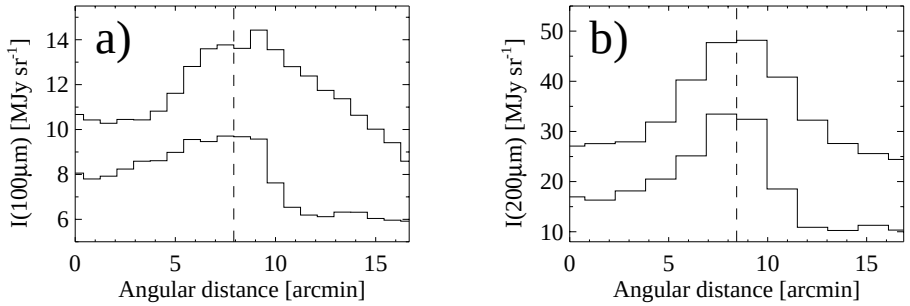

Fig. 2a and b. Surface brightness profiles across the TPN at 100 μm (**a**) and 200 μm (**b**). The upper profiles are along a constant right ascension (from east to west), the lower ones are along a constant declination (from south to north) with offsets of -4 and -15 MJy sr^{-1} at 100 and 200 μm, respectively, as indicated in Figs. 1 **c** and **d**. The dashed lines mark the optical center of the TPN where the two scans cross

still preliminary, it has been checked against COBE/DIRBE[1] (Diffuse InfraRed Background Experiment) annual average data, which have a pixel size of $0.32\times0.32^\circ$, i.e. half of the DIRBE field of view. The DIRBE data have been first color corrected for an $I_\lambda \propto \lambda^{-2}B(\lambda, T = 18\,\mathrm{K})$ spectral energy distribution. Then the surface brightness at the ISOPHOT bands has been estimated by fitting the DIRBE data at 100, 140 and 240 μm with a modified blackbody $\lambda^{-2}B(\lambda, T)$. At 100 μm we used also the IRAS ISSA data as an interconnecting step, in order to gain a better angular resolution than provided by the DIRBE data. The scale factor between the intensity values of DIRBE and ISSA data near the TPN has been derived by fitting the DIRBE-ISSA relationship with a straight line, giving I(DIRBE)=0.81 I(ISSA). The DIRBE based calibration at 200 μm is in good agreement (within $\sim$5%) with the internal ISOPHOT calibration. At 100 μm there is a difference of $\sim$50% between these two calibrations. We have adopted the DIRBE based calibration at both wavelengths. The calibration accuracy of the data presented in this paper is estimated to be 20%.

The determination of the surface brightness of the TPN over the background is a differential measurement, therefore no knowledge of the zodiacal light brightness is needed. However, the determination of the background surface brightness requires a subtraction of the zodiacal light. The zodiacal light brightness for the ecliptic coordinates of the TPN measurement, $I(100\,\mu\mathrm{m}) = 2.0\pm0.4$ and $I(200\,\mu\mathrm{m}) = 0.6\pm0.1$ MJy sr^{-1} at $\lambda-\lambda_\odot = 100^\circ$, $\beta = -62^\circ$, was derived from the DIRBE zodiacal light model (Reach et al. 1996; for a graphical presentation see Leinert et al. 1998).

In the following we mark the total surface brightness values (zodiacal light subtracted) as I, and the brightness above the background as ΔI. The subscripts *em* and *ext* used in the context of optical depths, are short for emission and extinction.

4. Results

4.1. Surface brightness distribution

The surface brightness maps at 100 and 200 μm are shown in Fig. 1, both as greyscale and contour maps. The grayscale image of surface brightness at R-band and a contour map of the ^{13}CO(J=1–0) column density are shown in Fig. 1e and f, respectively. The 200 μm distribution has a close resemblance to the ^{13}CO column density map, i.e. the relatively dense gas. On the other hand, the 100 μm distribution is broader and traces the whole dust distribution as revealed e.g. by the optical surface brightness image, i.e. scattered light. The 200 μm emission is more tightly confined around the center of the TPN. The diffuse dust which extends to south and west from the TPN, giving the cloud a cometary look at visual wavelengths (Lehtinen et al. 1995), is also seen in far-IR images especially at 100 μm. Surface brightness profiles across the center of the TPN are shown in Fig. 2. In the 100 μm map, where the angular resolution is sufficient to study the surface brightness distribution in detail, the intensity is fairly constant over much of the TPN, and it monotonically decreases towards the cloud edges, i.e. the TPN shows limb darkening.

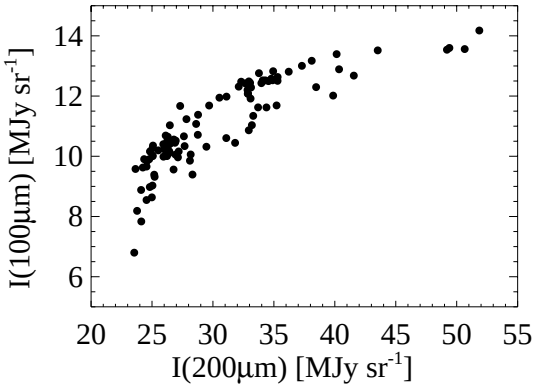

Fig. 3. The 100 μm surface brightness as a function of the 200 μm surface brightness. The points on the left-hand side correspond to the surroundings of the TPN whereas points on the right-hand side correspond to the TPN itself

In Fig. 3 are shown the C100 pixel values as a function of the C200 pixel values for the whole map area. The 100 μm surface brightness does not increase all the way to the center of the TPN, but reaches a saturation value of about 13 MJy sr^{-1}. This behaviour is suggestive of a temperature drop towards the cloud center, which causes the maximum of the blackbody radiation to move towards longer wavelengths.

[1] The COBE datasets were developed by the NASA Goddard Space Flight Center under the guidance of the COBE Science Working Group and were provided by the NSSDC

Table 2. The observed surface brightness and temperature of dust as derived using Eq. 1. The values at centre and annulus are values after subtracting the background at 100 and 200 μm (as given in the last line). The zodiacal light has been subtracted from the "background" values

Position	$I(100\,\mu\mathrm{m})$ [MJy sr^{-1}]	$I(200\,\mu\mathrm{m})$ [MJy sr^{-1}]	$T(\alpha=2)$ [K]	$T(\alpha=1)$ [K]
Centre	3.8 ± 0.8	24.4 ± 4.9	13.5 ± 1.1	15.5 ± 1.6
Annulus	2.3 ± 0.5	11.2 ± 2.2	14.6 ± 1.2	17.0 ± 1.7
Background	9.9 ± 2.0	25.9 ± 5.2	16.3 ± 1.3	19.4 ± 1.9

4.2. Dust temperature

The temperature of the dust has been determined by regridding first the C100 map to the resolution of the C200 map, and then fitting the C100 and C200 data, pixel by pixel, with a modified blackbody of the form

$$I(\lambda) \propto \lambda^{-\alpha} B(\lambda, T_{\mathrm{dust}}) \quad (1)$$

where α is the dust emissivity power law index, and $B(\lambda, T_{\mathrm{dust}})$ is the Planck function. In reality, there are grains of different composition and size, and due to extinction in the TPN, they are exposed to different radiation fields. Thus there are grains at different temperatures. The temperature determined via Eq. 1 is the temperature of the dominant far-IR emitters at the 100-200 μm range. E.g. in the interstellar dust model of Mathis et al. (1977) (hereafter called MRN dust model) they are small graphite particles, which are the dominant absorbers of the ISRF at UV-visual wavelengths, and thus are warmer than the silicate grains (Mezger et al. 1982; Draine & Lee 1984).

The temperature of the dust at the cloud center (a mean value over 2×2 pixel area), in the annulus (one pixel wide region outside the center), and at background (mean value around the TPN, excluding the 'tail' south-west of the TPN) are given in Table 2. For the central and annulus areas the intensities and temperatures are for the background-subtracted TPN contribution. The fitted modified blackbody function at the center of the cloud is shown in Fig. 4 as I_{emit}. The maximum of the function I_ν is located at $\sim 210\,\mu$m.

The excitation temperature of CO molecules in the TPN is ∼6.6 K (Lehtinen et al. 1995), regarded as a good estimate of the gas kinetic temperature. The temperature difference between gas and dust shows that they are not thermally coupled through collisions; this is as expected for maximum density $n(\mathrm{H_2}) \sim 10^4\,\mathrm{cm^{-3}}$ in the TPN. The gas and dust are expected to become thermally coupled only for densities greater than $\sim 10^5 - 10^6\,\mathrm{cm^{-3}}$.

4.3. Far-infrared opacity

In this section we shall derive the ratio between the far-infrared optical depth $\tau_{\mathrm{em}}(\lambda)$ and the hydrogen column density, i.e. the average absorption cross section per H-atom,

$$\sigma_\lambda^{\mathrm{H}} = \frac{\tau_{\mathrm{em}}(\lambda)}{N(\mathrm{H})} \quad (2)$$

If this ratio can be assumed to be the same from cloud to cloud, one can estimate the total cloud masses by using only the observed far-IR fluxes and the dust temperature derived from these fluxes (Hildebrand 1983).

In the case of optically thin emission ($\tau_{\mathrm{em}}(\lambda) \ll 1$) and an isothermal cloud, the observed surface brightness is

$$I(\lambda) = (1 - \mathrm{e}^{-\tau_{\mathrm{em}}(\lambda)}) B(\lambda, T_{\mathrm{dust}}) \approx \tau_{\mathrm{em}}(\lambda) B(\lambda, T_{\mathrm{dust}}) \quad (3)$$

The far-IR optical depths derived by using Eq. 3 are valid only if the intensity is proportional to the column density of dust. As discussed in Sect. 5.1. this proportionality is true in the case of the TPN.

In the case of α=2 we have an optical depth through the cloud center of $(1.0^{+0.8}_{-0.5})\,10^{-3}$, and $(4.0^{+3.3}_{-1.9})\,10^{-3}$, and in the case α=1 we have $(5.0^{+4.0}_{-2.4})\,10^{-4}$ and $(10.0^{+8.1}_{-4.7})\,10^{-4}$ at 200 μm and 100 μm, respectively. The extinction through the TPN at optical and near-IR wavelengths has been derived by using the near-IR extinction measurements of background stars by Lehtinen & Mattila (1996). To be compatible with the ISOPHOT data, we first smoothed the resolution of the extinction data to the resolution of the C200 data. Over the central 2×2 pixel area (180″×180″) of the 200 μm map we find an average K-band extinction of $A_{\mathrm{K}} = 0\overset{\mathrm{m}}{.}24 \pm 0\overset{\mathrm{m}}{.}05$, corresponding to $A_{\mathrm{V}} = 1\overset{\mathrm{m}}{.}9 \pm 0\overset{\mathrm{m}}{.}4$ (assuming that $R_{\mathrm{V}} = A_{\mathrm{V}}/E(B-V) = 5.0$). The ratios of the optical depths between far-infrared wavelengths and 2.2 μm are thus $\tau_{\mathrm{em}}(100)/\tau_{\mathrm{ext}}(2.2) = (1.8^{+2.4}_{-1.0})\,10^{-2}$, and $\tau_{\mathrm{em}}(200)/\tau_{\mathrm{ext}}(2.2) = (4.5^{+5.8}_{-2.7})\,10^{-3}$, for $\alpha = 2$. These values correspond to ratios $\tau_{\mathrm{em}}(100)/\tau_{\mathrm{ext}}(V) = (2.3^{+3.0}_{-1.2})\,10^{-3}$, and $\tau_{\mathrm{em}}(200)/\tau_{\mathrm{ext}}(V) = (5.7^{+7.3}_{-3.4})\,10^{-4}$, again for $R_{\mathrm{V}} = 5.0$.

We can use the near-IR extinction for estimating the total hydrogen column densities, $N(H + H_2)$, in the TPN. We adopt as a starting point the value $N(H + H_2)/E(B-V) = 5.8\,10^{21}\,\mathrm{cm^{-2}\,mag^{-1}}$ for diffuse clouds (Bohlin et al. 1978) together with $A_{\mathrm{K}}/E(B-V) = 0.335$ (Mathis 1990, "diffuse dust") to obtain $N(H + H_2)/A_{\mathrm{K}} = 1.7\,10^{22}\,\mathrm{cm^{-2}\,mag^{-1}}$. In view of the similarity of the diffuse cloud and dense cloud extinction curves for $\lambda > 0.7\,\mu$m it appears reasonable to adopt this value of $N(H + H_2)/A_{\mathrm{K}}$ as a first approximation also for the dense cloud extinction. We thus derive for the TPN the total hydrogen column density $N(H+H_2) = 4.2 \pm 1.0\,10^{21}$ H-atoms cm^{-2}. The calculated values of $\sigma_\lambda^{\mathrm{H}}$, derived using Eq. (2), are shown in Table 3, together with some values from literature.

It is obvious that the Bohlin et al. (1978) relationship, which is frequently used (e.g. in the papers cited in Table 3) in "scaling" the dust column densities to $N(H + H_2)$, may be seriously in error for the case of dense clouds. For a more detailed discussion see e.g. Mathis (1990).

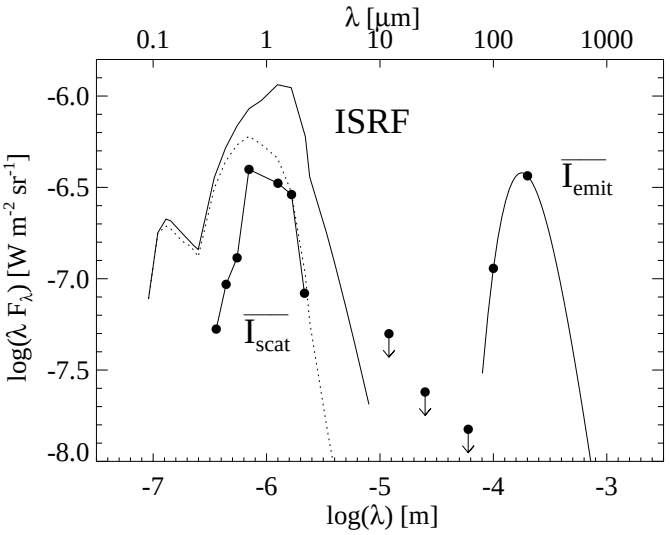

Fig. 4. The spectral energy distribution of the emitted radiation $\overline{I_{\rm emit}}$ and the scattered radiation $\overline{I_{\rm scat}}$. The upper limits of the IRAS 12, 25 and 60 μm emission at 2 σ level are indicated with an arrow. The mean intensity of the ISRF between 0.0912–8.0 μm is shown for comparison (according to Mathis et al. (1983) and Lehtinen & Mattila (1996)). The ISRF plotted with a dotted line is the portion of the ISRF that suffers extinction in the TPN

Table 3. The derived average absorption cross sections per H-atom at 100 and 200 μm, for dust emissivity power law index α=1 and 2. Some values taken from literature are also shown

α	$\sigma^{\rm H}_{100\,\mu{\rm m}}$ [cm^2 H-atom^{-1}]	$\sigma^{\rm H}_{200\,\mu{\rm m}}$ [cm^2 H-atom^{-1}]	Reference
1	$(2.4^{+3.3}_{-1.4})\,10^{-25}$	$(1.2^{+1.6}_{-0.7})\,10^{-25}$	This study
2	$(9.5^{+13.5}_{-5.5})\,10^{-25}$	$(2.5^{+3.2}_{-1.4})\,10^{-25}$	
1		$(1.7-4.0)\,10^{-26}$	Laureijs et al.
2		$(4.2-9.5)\,10^{-26}$	(1996)
	$2.7\,10^{-25}$ (silic.)	$6.6\,10^{-26}$	Draine & Lee
	$3.5\,10^{-25}$ (grap.)	$9.5\,10^{-26}$	(1984), MRN
	$6.2\,10^{-25}$ (total)	$1.6\,10^{-25}$	size distribution
		$1.7\,10^{-25}$	Hildebrand (1983)
	$8.0\,10^{-25}$	$2.5\,10^{-25}$	Désert et al. (1990)

5. Discussion

5.1. Heating by the ISRF

The interstellar radiation field is the heating source of the dust grains in globules without internal heating sources. The grains absorb ultraviolet and optical photons, and subsequently emit photons at far-infrared wavelengths corresponding to the equilibrium dust temperature. The fraction of the ISRF that suffers extinction in the TPN is calculated by taking into account the wavelength and spatial dependence of the optical depth through the TPN. Let us consider a ray of incident radiation that goes through a spherical cloud, and intersects the surface at an angle θ to the normal. Let $\mu = \cos\theta$. The fraction of this radiation that suffers extinction is $(1-\exp(-\tau(\mu,\lambda)))$, where $\tau(\mu,\lambda)$ is the optical depth through the cloud along the ray.

The flux of the ISRF that suffers extinction is then

$$F^{\rm ext}_{\rm ISRF}(\lambda) = 2\,\pi\,I_{\rm ISRF}(\lambda)\int_0^{+1}(1-{\rm e}^{-\tau(\mu,\lambda)})\,\mu\,{\rm d}\mu \qquad (4)$$

where $I_{\rm ISRF}(\lambda)$ is the isotropic radiation intensity. The luminosity provided by the ISRF for the cloud is then

$$\begin{aligned} L_{\rm ISRF} &= 4\,\pi\,r^2\int F^{\rm ext}_{\rm ISRF}(\lambda)\,{\rm d}\lambda \qquad (5)\\ &= 4\,\pi^2\,r^2\int I_{\rm ISRF}(\lambda)\,[2\int_0^{+1}(1-{\rm e}^{-\tau(\mu,\lambda)})\,\mu\,{\rm d}\mu]\,{\rm d}\lambda\\ &\equiv 4\,\pi^2\,r^2\,I^{\rm ext}_{\rm ISRF}\end{aligned}$$

where r is the radius of the cloud and $I^{\rm ext}_{\rm ISRF} = F^{\rm ext}_{\rm ISRF}/\pi$. The term in the square brackets in the Eq. (5) is the fraction of the ISRF that suffers extinction in the cloud. For the TPN its value at each wavelength over a circular region with a radius r=1.7′, an area which corresponds to the area over the four centermost pixels at 200 μm, has been calculated by using the known optical depth-impact parameter relation from Lehtinen & Mattila (1996). We have estimated the local $I_{\rm ISRF}(\lambda)$ between 0.091–8.0 μm by using Table A3 of Mathis et al. (1983), except between 1.2–2.2 μm where we have adopted the average sky brightness values of Lehtinen & Mattila (1996) based on COBE/DIRBE data at 1.25, 1.65 and 2.2 μm. Integrating over wavelength, we obtain the total ISRF intensity that suffers extinction in the TPN
$I^{\rm ext}_{\rm ISRF} = 1.0\,10^{-6}\,{\rm W\,m^{-2}\,sr^{-1}}$.

The energy emitted by dust as a modified black-body radiation is

$$L_{\rm emit} = 4\,\pi\,r^2\,F_{\rm emit} = (4\,\pi\,r^2)\,\pi\int\overline{I_{\rm emit}}(\lambda)\,{\rm d}\lambda \qquad (6)$$

where $F_{\rm emit}$ is the far-infrared flux and $\overline{I_{\rm emit}}(\lambda)$ is the mean far-infrared surface brightness of the cloud averaged over the disk. By integrating the fitted modified black-body function for α=2 over wavelength, we obtain a total surface brightness of
$\overline{I_{\rm emit}} = (4.0^{+0.5}_{-0.8})\,10^{-7}\,{\rm W\,m^{-2}\,sr^{-1}}$.

Due to the non-zero value of the dust albedo, not all the energy of the ISRF is absorbed by the dust grains. The energy not absorbed is scattered from the cloud by the dust particles, and it manifests itself as a surface brightness at optical and near-IR wavelengths. For the TPN surface brightness observations exist at U, B, V, R (FitzGerald et al. 1976) and J, H, K (Lehtinen & Mattila 1996) bandpasses. To be consistent with the determination of $I^{\rm ext}_{\rm ISRF}$ above, we have calculated the mean of the surface brightness over a circular region with radius $r = 1.7'$. Integrating between U and K bandpasses we have the mean intensity of scattered radiation
$\overline{I_{\rm scat}} = 4.9\,10^{-7}\,{\rm W\,m^{-2}\,sr^{-1}}$.

The luminosity of the scattered radiation, $L_{\rm scat}$, is calculated in analogy to Eq. (6). The spectral energy distributions of the

emitted ($\overline{I_{\rm emit}}$) and scattered ($\overline{I_{\rm scat}}$) radiation, the ISRF, and the IRAS 12, 25 and 60 μm upper limits are shown in Fig. 4. The ISRF curve plotted as a solid line is the un-attenuated local ISRF, while the dotted line is the portion of the ISRF that suffers extinction in the TPN. In this diagram the sum of the areas under the $\overline{I_{\rm emit}}$ and $\overline{I_{\rm scat}}$ curves should be equal to that under the ISRF spectrum that suffers extinction in the TPN (dotted line).

For the ratio $L_{\rm ISRF}/(L_{\rm emit}+L_{\rm scat})$ we have

$$R \equiv \frac{L_{\rm ISRF}}{L_{\rm emit}+L_{\rm scat}} = \frac{I^{\rm ext}_{\rm ISRF}}{\overline{I_{\rm emit}}+\overline{I_{\rm scat}}} \quad (7)$$

which is independent of the distance of the TPN. Using the values calculated above we obtain $R \sim 1.1$. This result shows that the ISRF is capable of providing all the energy that is scattered or emitted as thermal emission by dust grains at far-IR.

The ratio of the scattered and emitted luminosities, $L_{\rm scat}/(L_{\rm emit}+L_{\rm scat}) = a_{\rm eff}$, is the effective albedo of the whole cloud. $a_{\rm eff}$ is always smaller than the single scattering albedo, a, due to multiple scattering in the cloud, provided that $a < 1.0$. We have used the Monte Carlo radiation transfer method of Lehtinen & Mattila (1996) to calculate $a_{\rm eff}$ for different values of a and the asymmetry parameter g at R-band, where the maximum of the SED for scattered radiation is located (see Fig. 4). We have to take into account that $\overline{I_{\rm emit}}$ is independent of the viewing direction, whereas $\overline{I_{\rm scat}}$ reflects the anisotropy of the incident radiation field smoothed, however, for large τ. It is found that for larger values of g the $a_{\rm eff}$ values decrease, because the photons have a higher probability of being absorbed after entering the inner, denser parts of the cloud. However, this decrease of $a_{\rm eff}$ is only about 9 % from $g = 0.0$ to $g = 0.9$. Using the observed values of $\overline{I_{\rm emit}}$ and $\overline{I_{\rm scat}}$ we calculate $a_{\rm eff} \approx 0.55$, which corresponds to a single scattering albedo of about 0.7, almost irrespective of the value of g. This value is in excellent agreement with the single scattering albedo of dust found by FitzGerald et al. (1976) for the TPN.

The far-IR thermal emission considered here is probably not the only form of dust emission from the TPN. Recent ISO observations have confirmed that the emission features and a continuum between ~3–20 μm (probably due to PAHs) are a ubiquitous feature of the emission of dust in the Galaxy (Mattila et al. 1996; Boulanger et al. 1996; Lemke et al. 1998). This mid-IR emission may account for 25% of the total radiation emitted by dust (Boulanger et al. 1985). Furthermore there is evidence of emission from very small grains at the IRAS 25 and 60 μm bands (Chlewicki & Laureijs 1988). Also taking into account these mid-IR contributions, the value of R approaches unity.

The far-IR surface brightness *distribution* of an externally heated globule is a valuable tool for determining the density and temperature distribution (Lee & Rogers 1987; Leung et al. 1989). In the case of an optically thin cloud at UV-optical wavelengths, the ISRF is able to heat the cloud throughout, and the cloud is isothermal. The observed intensity is thus proportional to the dust column density and the cloud shows limb darkening. In the case of a homogeneous cloud which is optically thick at UV-optical wavelengths ($\tau \gtrapprox 10$), the ISRF mainly heats the outer layers of the cloud, up to a depth which is about one mean free path of the UV-optical photons measured from the cloud surface. The cloud has a cold interior and a warmer outer shell. The observed intensity at far-IR wavelengths is mainly determined by the dust temperature along the line of sight, not by the dust column density; the cloud shows limb brightening.

The behaviour of the ratio I(100 μm)/I(200 μm) (Fig. 3) indicates a temperature drop towards the center of the TPN. However, because of the absence of limb brightening at far-IR, we conclude that there is no pronounced cold core - warm shell structure. This is compatible with the centrally condensed dust density distribution (Lehtinen & Mattila 1996), which enables the UV-optical photons to penetrate deeper into the cloud than in the homogeneous case, and consequently the temperature decrease towards the cloud center is less pronounced.

5.2. Dust properties

Draine & Lee (1984) have calculated absorption cross sections using the Mathis et al. (1977, MRN) dust model. The resulting $\sigma^{\rm H}_{100\,\mu{\rm m}}$ and $\sigma^{\rm H}_{200\,\mu{\rm m}}$ values are given in Table 3 for each of the MRN grain components, i.e. graphite and silicate particles, as well as for the total mixture. It can be seen that the calculated MRN cross sections are in good agreement with the TPN values for $\alpha = 2$. This value of α also results from the MRN model (see Draine & Lee 1984). For comparison with the observations one has to take into account that the observationally determined cross section is a weighted sum of the graphite and silicate cross sections, the weight factor for the warmer graphite particles being larger than the one for the cooler silicates. Thus the effective cross section will be between the "graphite" and "silicate" values (Mezger et al. 1982).

We give in Table 3 also the estimate of Hildebrand (1983) for $\sigma^{\rm H}_{200\,\mu{\rm m}}$. It agrees with our observational result for $\alpha = 2$.

Désert et al. (1990) have developed a dust model composed of big grains, very small grains and PAHs. The values of $\sigma^{\rm H}_{\lambda}$, estimated from their Fig. 3, are in excellent agreement with our values.

The derived characteristic dust temperature in the TPN, 14–16 K, is in good agreement with the value of the characteristic dust temperature of $\simeq 14$ K for graphite grains in globules as derived by Mezger et al. (1982) and Draine & Lee (1984).

Bernard et al. (1992) have modelled the IR emission from dust clouds heated only by the ISRF. They used the ISRF determined by Mathis et al. (1983) between UV and near-IR wavelengths, adding the large scale IR emission from the galactic plane. According to their model the surface brightness at the cloud center increases proportionally with the adopted visual extinction of the cloud, $A_{\rm V}$, until $A_{\rm V} \simeq 4-6$ mag, where the surface brightness attains its maximum. Their cloud models which have the characteristics closest to the TPN, have a 100 μm surface brightness at the cloud center of about 18 MJy sr^{-1}. This result is not consistent with the observed value of $\Delta I(100\,\mu{\rm m}) \approx 4$ MJy sr^{-1} at the center of the TPN. This discrepancy could simply be explained by assuming that the intensity of the ISRF

impinging on the TPN is less than assumed in the models. However, as shown by the energy balance calculations in Sect. 5.1, the energy input into the TPN, in the form of ISRF, cannot be less than the integrated intensity of the ISRF in the solar neighbourhood. One solution is that the dust grains in the TPN are colder because they are bigger than in the model of Bernard et al. (1992). Thus, the bulk of the spectral energy distribution of emission shifts towards longer wavelengths, reducing the emission at 100 μm. The near-IR dust albedo determination of Lehtinen & Mattila (1996) has also indicated that there are bigger dust grains in the TPN than in the diffuse interstellar medium.

6. Conclusions

We have presented imaging of a quiescent globule at 100 and 200 μm with the ISOPHOT far-IR camera aboard ISO (Infrared Space Observatory). The characteristic dust temperature is between 13.5–15.5 K, assuming that the dust emission has the form of a modified blackbody, $I(\lambda) \propto \lambda^{-\alpha} B(\lambda, T_{\rm dust})$, and α between 1–2.

The surface brightness observations indicate that the TPN does not have a distinct cold core - warm envelope structure.

The energy balance of dust in the cloud has been studied by considering three factors: the energy input from the general ISRF, and energy outputs in the form of scattered radiation (from optical to near-IR wavelengths) and emitted radiation (at far-IR wavelengths). The method applied here is independent of the distance of the TPN. It has been found that the ratio between energy input and output is ~ 1.1, which means that the ISRF is sufficient to be the main heat source of dust. Thus, we do not encounter the puzzling situation as in previous observations, which indicated that the far-IR emission alone from a sample of quiescent globules was larger than the ISRF intensity.

Acknowledgements. We gratefully acknowledge the funding of the ISOPHOT experiment by the Deutsche Agentur für Raumfahrtangelegenheiten (DARA) and financial support for this research project by the Max-Planck Society. K.L. thanks the staff for hospitability during his stays at Max-Planck-Institut für Astronomie, in Heidelberg. K.L. thanks Christian Surace for the flatfielding program. The work of K.L. has been supported by the Vilho, Yrjö and Kalle Väisälä foundation of the Finnish Academy of Science and Letters, and K.L., K.M. and L.K.H. by the Finnish Academy through grant No. 1011055. We thank Alison Rushworth for checking the grammar. We thank the referee, Dr. J. Mathis, for comments which clarified this article.

References

Bernard J.P., Boulanger F., Desert F.X., Puget J.L. 1992, A&A 263, 258
Bohlin R.C., Savage B.D., Drake J.F. 1978, ApJ 224, 132
Boulanger F., Baud B., van Albada G.D. 1985, A&A 144, L9
Boulanger F., Reach W.T., Abergel A., et al. 1996, A&A 315, L325
Chlewicki G., Laureijs R.J. 1988, A&A 207, L11
Clemens D.P., Yun J.L., Heyer M.H. 1991, ApJS 75, 877
Désert F.-X., Boulanger F., Puget J.L. 1990, A&A 237, 215
Draine B.T., Lee H.M. 1984, ApJ 285, 89
FitzGerald M.P., Stephens T.C., Witt A.N. 1976, ApJ 208, 709
Gabriel C., Haas M., Heinrichsen I., Tai W.-M. 1996, The ISOPHOT Interactive Analysis-PIA User Manual
Hildebrand R.H. 1983, QJRAS 24, 267
Keene J. 1981, ApJ 245, 115
Keene J., Harper D.A., Hildebrand R.H., Whitcomb S.E. 1980, ApJ 240, L43
Keene J., Davidson J.A., Harper D.A., et al. 1983, ApJ 274, L43
Laureijs R.J., Haikala L., Burgdorf M., et al. 1996, A&A 315, L317
Lee M.H., Rogers C. 1987, ApJ 317, 197
Leung C.M., O'Brien E.V., Dubisch R. 1989, ApJ 337, 293
Lehtinen K., Mattila K. 1996, A&A 309, 570
Lehtinen K., Mattila K., Schnur G.F.O., Prusti T. 1995, A&A 295, 487
Leinert Ch., Bowyer S., Haikala L.K., et al. 1998, A&AS, 127, 1
Lemke D., Klaas U., Abolins J., et al. 1996, A&A 315, L64
Lemke D., Mattila K., Lehtinen K., et al. 1998, A&A in press
Mathis J.S. 1990, ARA&A 28, 37
Mathis J.S., Rumpl W., Nordsieck K.H. 1977, ApJ 217, 425
Mathis J.S., Mezger P.G., Panagia N. 1983, A&A 128, 212
Mattila K., Lemke D., Haikala L.K., et al. 1996, A&A 315, L353
Mezger P.G., Mathis J.S., Panagia N. 1982, A&A 105, 372
Mezger P.G. 1991, in Bowyer S., Leinert Ch. (eds) The Galactic and Extragalactic Background Radiation, Kluwer, Dordrecht, p. 63
Reach W.T., Franz B.A., Kelsall T., Weiland J.L. 1996, in "Unveiling the cosmic infrared background", E.Dwek, ed. AIP Conf. Proc. 348, Woodbury, p.37
Yun J.L., Clemens D.P. 1991, ApJ 381, 474